PCCP

Accepted Manuscript

ROYAL SOCIETY OF CHEMISTRY

www.rsc.org/pccp

Phys. Chem. Chem. Phys RSC Publishing

PAPER

Surface oxygen-vacancy induced photocatalytic activity of $La(OH)_3$ nanorods prepared by a fast and scalable method

Received (in XXX, XXX) Xth XXXXXXXXX 20XX,

Accepted Xth XXXXXXXXX 20XX

DOI: 10.1039/b000000x

Fan Dong [a,c]* Xiang Xiao [a], Guangming Jiang [c], Yuxin Zhang [d], Wen Cui [a], Jinzhu Ma [b,]*

[a] *Chongqing Key Laboratory of Catalysis and Functional Organic Molecules, College of Environmental and Biological Engineering, Chongqing Technology and Business University, Chongqing, 400067, China.*

[b] *Research Center for Eco-Environmental Sciences, Chinese Academy of Sciences, Beijing 100085, China.*

[c] *Engineering Research Center for Waste Oil Recovery Technology and Equipment, Ministry of Education, Chongqing Technology and Business University, Chongqing, 400067, China.*

[d] *College of Materials Science and Engineering, Chongqing University, Chongqing, 400044, China.*

Uniform one-dimensional defective $La(OH)_3$ nanorods were synthesized by a facile, fast and scalable method. This simple method avoids treatment at high temperature, utility of surfactants or templates, and can be finished within a short time. The results indicate that oxygen-vacancies were formed in $La(OH)_3$ nanorods, which could extend the photoresponse range. The XPS, PL, solid state ESR measurement and DFT calculation revealed the pivotal role of oxygen-vacancy on the formation of impurity level in the band gap of $La(OH)_3$. The as-prepared $La(OH)_3$ nanorods exhibited an efficient photocatalytic activity in removal of NO at ppb-level under ultraviolet illumination. The highly enhanced photocatalytic activity of $La(OH)_3$ nanorods could be ascribed to the synergy of the lower impurity level below conduction band and the high separation efficiency of photogenerated electron-hole pairs. DMPO-ESR spin trapping results imply that the hydroxyl radicals are the main reactive species that are responsible for NO photooxidation. On the basis of combined experimental and theoretical investigation, an oxygen vacancy-mediated photocatalysis mechanism of defective $La(OH)_3$ nanorods was proposed. This work could not only provide a fast and environmentally friendly approach for synthesis of nanostructured photocatalysts, but also new insights into the understanding of the role of vacancy in semiconductor photocatalysis.

1. Introduction

Shape and dimensionality are regarded as important factors which determine the chemical and physical properties of catalytic materials. Among the various nanostructures, it is generally accepted that one dimensional (1D) nanostructures could provide a good system to investigate the dependence of physicochemical property on dimensionality and size reduction. 1D nanostructure (such as wires, rods, tubes and belts) has become the focus of intensive research because of their potential applications in mesoscopic physics, nanoscale devices, sensors, catalysis and environment .[1-5]

Lanthanide compounds have unique electronic structure and exhibit a number of transition modes involving the 4f shell of the atoms/ions. One-dimensional lanthanide hydroxides ($La(OH)_3$) has been of growing interest owing to the promising applications in sensors,[6] catalyst,[7,8] and capacitors.[9] Various synthesis techniques have been adopted for the preparation of $La(OH)_3$ nanostructures, including solvothermal,[10] hydrothermal,[11,12] precipitation,[13] and composite-hydroxide-mediated (CHM) methods.[6] However, these preparation methods generally need the use of surfactants/templates or complicated reaction conditions to get the desired shape/structure.

Semiconductor photocatalysis is developing into one of the most promising technologies for environmental remediation and solar energy conversion.[14,15] It is well known that the photocatalytic performance of one material is mainly governed by the microstructures including crystal structure, morphology, defect, and band structure. Among these factors, making defects in photocatalysts has been found to be an effective method for improving the activity via changing the charge transfer and band structure.[16,17] Especially, oxygen-vacancy can serve as photoinduced charge traps and modify the band structure of semiconductor photocatalysts, which is conductive to the enhanced photocatalytic activity.[18-20] The light absorption range of semiconductor materials can be enhanced or expanded by introducing oxygen vacancies, which result in the extended light absorption spectra and band gap narrowing.[18,21] Recently, oxygen-vacancy associated properties have been widely surveyed in simple semiconductors, such as TiO_2 ,[18-19, 20, 22] Fe_2O_3 ,[23] and ZnO.[24-26] However, to the best of knowledge, the oxygen vacancies in $La(OH)_3$ and their influence on the band structure and photocatalytic activity have seldom been investigated.

Herein, we present a template-free and facile precipitation method to fabricate uniform one-dimensional $La(OH)_3$ nanorods at room temperature. The synthesis is carried out in aqueous medium using $La(NO_3)_3 \cdot 6H_2O$ and ammonia as precursors and can be finished within 1.5 h. The photocatalytic activity and stability of the product is evaluated by removal of NO in air

under the irradiation of UV light (280 nm). The $La(OH)_3$ nanorods exhibit an efficient photocatalytic activity for NO removal. The photocatalysis mechanism is investigated based on combined experimental and theoretical calculation. The band gap of $La(OH)_3$ nanorods is as broad as 4.64 eV (about 265nm) that cannot be excited by 280 nm UV light. The formation of oxygen-vacancy extends the photoresponse of $La(OH)_3$ nanorods. DFT calculation and solid state ESR measurement indicate that the expanded absorption photoresponse of $La(OH)_3$ nanorods can be ascribed to the formation of new impurity level below the conduction band. The present work demonstrates a facile, fast and scalable method for high quality $La(OH)_3$ nanorods with oxygen-vacancies that can be used as an excellent photocatalysts for environmental application and solar energy conversion

2. Experimental Section

2.1. Preparation

All the chemicals used were analytical grade and used without any further purification. In a typical synthesis, appropriate amounts of $La(NO_3)_3$•$6H_2O$ (1.083 g) were dissolved in 120 ml distilled water in a graduated cylinder, and a concentrated ammonia solution (28 wt.%, 15 mL) was added dropwise with magnetic stirring for 30 min. The precursor solution was thermal aging in 25 ℃ in water bath for 1 h. Subsequently, the product was centrifuged and washed with distilled water and ethanol for four times and dried at 60 ℃ to get the final $La(OH)_3$ nanorods. The obtained sample was labeled as La-25. The time for the whole synthesis can be controlled within 1.5 h.

Hydrothermal method is chosen as the control experiment. The same amount of $La(NO_3)_3$ $6H_2O$ were dissolved in 40 ml distilled water with continuous stirring. Then a concentrated ammonia solution (28 wt%, 20 mL) was added with magnetic stirring. Distilled water was added to the above solution to make the total volume of 70 ml and stirred for 30 min. Afterward, the obtained solution was transferred to a 100 ml Teflon-lined autoclave. The precursor solution was hydrothermally treated at 150 ℃ for 8 h. After the hydrothermal reaction, the product was centrifuged and washed to get the final $La(OH)_3$. The obtained sample was labeled as La-150.

2.2. Characterization

The crystal phases of the sample were analyzed by X-ray diffraction with Cu–Kα radiation (XRD: model D/max RA, Rigaku Co., Japan). In order to characterize the morphology and structure of the obtained products, scanning electron microscope (SEM: JEOL model JSM-6490, Japan) and transmission electron microscope (TEM: JEM-2010, Japan) were used to collect the SEM and TEM images. The Brunauer–Emmett–Teller (BET) specific surface area (S_{BET}) and pore structure of the samples were analyzed by Nitrogen adsorption-desorption in a nitrogen adsorption apparatus (ASAP 2020, USA, with all samples degassed at 100 ℃ for 12 h prior to measurements. The UV-vis diffuse reflection spectra were obtained for dry-pressed disk samples using a Scan UV-Vis spectrophotometer (UV–Vis DRS: UV-2450, Shimadzu, Japan) equipped with an integrating sphere assembly, using $BaSO_4$ as a reflectance sample. The electron spin resonance (ESR) signals of hydroxyl radicals spin-trapped by spin-trap reagent 5, 5-dimethyl-1-pirroline-N-oxide (DMPO) in water were examined on a Bruker model EPR JES-FA200 spectrometer equipped with a quanta-Ray Nd:YAG laser system as the irradiation source. The ESR measurement of photocatalyst powder for vacancies was carried out using an Endor spectrometer (JEOL ES-ED3X) at 77 K. The g factor was obtained by taking the signal of manganese. The Photoluminescence (PL: F-7000, HITACHI, Japan, was used to investigate the optical properties of the obtained samples.

2.3. Computational details

DFT calculations were performed using CASTEP package on the basis of the plane-wave-pseudo-potential approach. The Perdew–Burke–Ernzerhof (PBE) of the generalized gradient approximation (GGA) was used as the exchange–correlation function. The interaction between valence electrons and the ionic core was described by the ultrasoft pseudo-potential. Calculations were carried out with a Monkhorst-Pack *k*-point mesh of (4×2×3) and a plane-wave cutoff of 380 eV.

A 56-atom supercell made up by 1×2×2 unit cell has been used to simulate an $La(OH)_3$ bulk crystal. The oxygen deficient $La(OH)_3$ was modeled by removing one oxygen atom in $La(OH)_3$ cells.The initial geometry configurations were optimized by the Broyden, Fletcher, Goldfarb and Shannom minimizer. The energetic convergence threshold for the self-consistent field (SCF) is 5.0×10^{-7} eV/atom. The convergence tolerance parameters of optimized calculations were a maximum energy of 5.0×10^{-6} eV/atom, a maximum force of 0.01 eV/Å, a maximum stress of 0.02 GPa and a maximum displacement of 0.0005 Å. After finishing the geometry optimizations, the band structures and the density of states (DOS) were calculated.

The oxygen vacancy formation energy is computed from

E_{vac}=E(oxygen deficient $La(OH)_3$)-E($La(OH)_3$)+1/2E(O_2),

where E(oxygen deficient $La(OH)_3$) is the total energy of $La(OH)_3$ with an oxygen vacancy, E($La(OH)_3$) is the total energy of $La(OH)_3$. The formation energy is referenced to half the total energy of molecular O_2

2.4. Evaluation of the ultraviolet light photocatalytic activity

The photocatalytic activity of the as-synthesized sample was evaluated by removing NO at ppb level in a continuous flow reactor. The rectangular reactor was made of stainless steel covered with Quartz-Glass, the volume of which was 4.5 L (30 cm×15 cm×10 cm). A 6 W commercial UV lamp (280 nm) was vertically placed outside and above the reactor. For each photocatalytic activity test, two sample dishes (with a diameter of 12.0 cm) containing 0.1 g of photocatalyst powder were placed in the center of reactor. The photocatalyst samples were prepared by coating aqueous suspension of the samples onto the glass dishes. The coated dish was treated at 70 ℃ to evaporate the water and then cooled to room temperature before the photocatalytic activity test. The NO gas was acquired from a compressed gas cylinder at a concentration of 100 ppm of NO (N_2 balance). The initial concentration of NO was diluted to 550 ppb by the air. The flow rate of air stream and NO were controlled at 2.4 L/min and 15 mL/min, respectively. Then the two gas streams were premixed by a three-way valve. After the adsorption-desorption equilibrium was achieved, the lamp was turned on. The concentration of NO was continuously measured by a chemiluminescence NO analyzer (Thermo Scientific, 42i-TL), which monitors NO, NO_2, and NOx (NOx represents NO + NO_2) with a sampling rate of 1.0 L min^{-1}.The removal ratio (η) of NO was calculated as η (%) = $(1 - C/C_0) \times 100\%$, where C and C_0 are the concentrations of NO in the outlet steam and the feeding stream, respectively.

3. Results and discussion

3.1. Phase structure

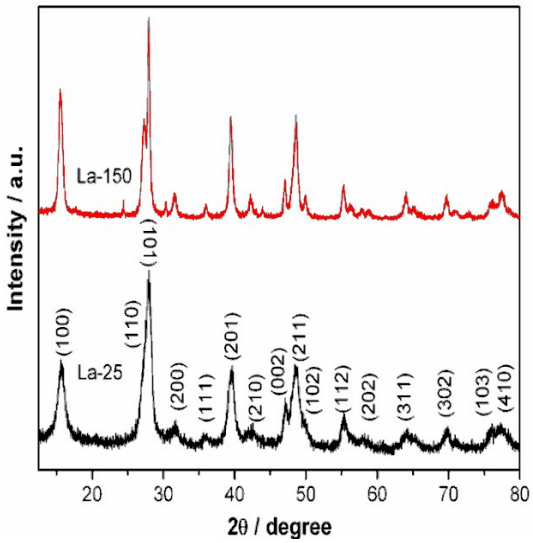

Fig. 1 XRD patterns of La-25 and La-150.

The XRD patterns of the as-prepared samples derived from different preparation methods are depicted in Fig. 1. All the diffraction peaks of the La-25 samples can perfectly match the standard card of $La(OH)_3$ (JCPDS-ICDD Card No. 36-1481). No other peaks can be detected, suggesting that the La-25 sample is highly pure in phase. The strongest peak at $2\theta=27.9^{o}$ is representative for (101) phase reflections. From the full width at half-maximum of the diffraction pattern, the crystal sizes can be calculated by using Scherrer's equation.[27] The crystal size of La-25 is calculated to be 8.0 nm. For La-150 sample prepared by hydrothermal method, the diffraction peaks occur at a stronger intensity and some impurity peaks can be observed. Obviously, the this facile and fast method for $La(OH)_3$ is not only simple in the preparation process, but could also provide more opportunities for the preparation of pure phase $La(OH)_3$. Furthermore, the peak intensities of La-25 are lower than those of the La-150, indicating that the crystallinity of La-25 is lower. Low crystallinity is favorable for the formation of defects .[28]

3.2. Morphology and texture

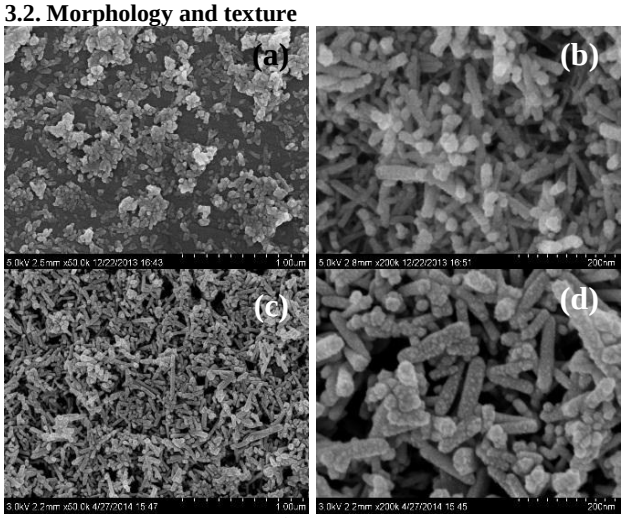

Fig. 2 SEM images of La-25(a, b) and La-150 (c, d).

The morphology and microstructure of the samples were characterized by SEM, TEM and HRTEM. Fig. 2 shows the SEM images of the samples obtained from different preparation methods. The SEM images of the La-25 in Fig. 2a and 2b show that La-25 consists of 1D nanorods which are uniformly dispersed. The average diameter of the $La(OH)_3$ nanorods is 15~20 nm. Fig. 2c and 2d display the SEM images of the La-150 obtained by hydrothermal processing. It is obvious that rod-like products are produced. The average diameter of the nanorods is 20~30 nm because the sample are better crystallized under hydrothermal treatment. However, the morphology of La-150 is irregular and most of the rods are aggregated together. Hence, the facile and fast precipitation method demonstrates significant advantages for the preparation of uniform $La(OH)_3$ nanorods.

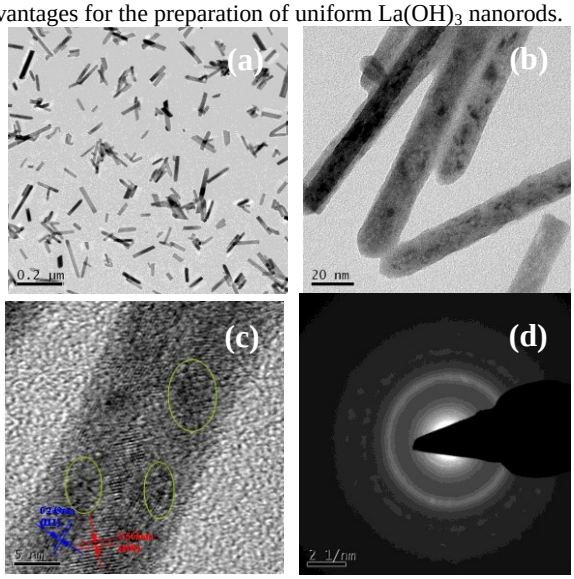

Fig. 3 TEM (a, b), HRTEM (c) and SAED (d) images of La-25.

TEM and high-resolution TEM (HRTEM) investigations give further information on the morphology and the structural features of La-25 nanorods. Fig. 3a and 3b shows the typical TEM images of La-25 of one-dimensional rod-like nanostructure. The diameter of the nanorods is 15–20 nm and the length is 50–200 nm. Fig. 3c shows the typical HRTEM image of La-25. The observed spacing between the lattice planes of the sample is measured to be 0.565 nm and 0.249 nm, corresponding to (100) and (111) crystallographic planes of $La(OH)_3$. The crystal in different orientations can be observed, which indicate that the prepared $La(OH)_3$ nanorods are polycrystalline. The $La(OH)_3$ nanorods are composed by numerous crystalline subunits with various orientations. The SAED image of a single nanorod (Fig. 3d) further implies that the nanorod is polycrystalline, which agrees well with the HRTEM results. In addition, the HRTEM image (Fig. 3c) reveals that part of the lattice fringes of La-25 crystal become indiscernible, which suggests that some of the region becomes disordered in La-25 crystal due to the formation of defects.

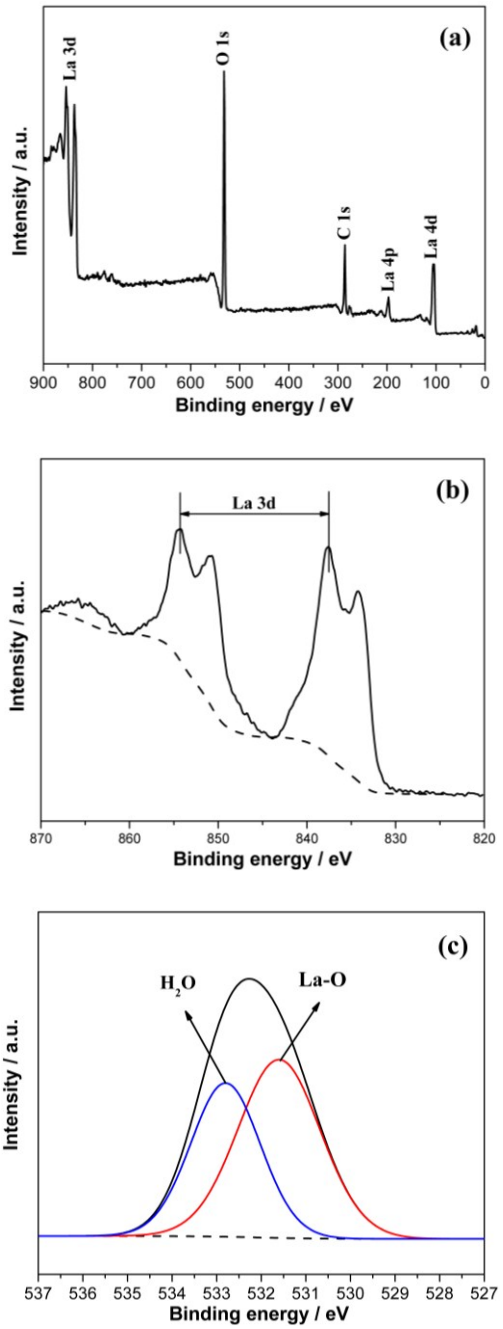

Fig. 4 XPS spectra of La-25 sample, survey (a), La 4d (b) and O 1s (c)

To further investigate the chemical state, XPS measurement was carried out. Fig. 4 shows the XPS spectra of La-25 sample. The survey spectra in Fig. 4a implies that the presence of La, O and C elements, where C comes from the adventious adventitious carbon species from the XPS measurement. Fig. 4b shows the typical La 3d3/2 XPS spectra. A double-peak structure with a peak energy of 837.0 eV and a satellite energy of 854.4 eV can be observed. The high binding energy of the satellite can be ascribed to the shake-up process associated with the O 2p → La 4f charge transfer.[29] The O1s XPS spectra can be fitted with two peaks ascribing to La-O and H_2O.[29] From Fig. 4c and 4b, the molar ratio of O/La can be determined, which is less than 3.0. This result indicates the formation of oxygen defects, consistent with the TEM observation in Fig. 3c.

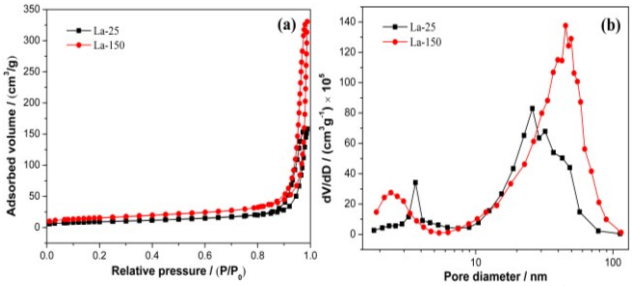

Fig. 5 N_2 sorption isotherms and pore size distribution curves of La-25 and La-150.

The N_2 sorption isotherms and pore size distribution curves of La-25 and La-150 are shown in Fig. 5. The two samples have similar isotherms of type V and hysteresis loops of type H3 at relative pressure range of 0.8 to 1.0 (Fig. 5a), which indicates the presence of mesopores (2-50 nm). The hysteresis loops of La-25 and La-150 approach $P/P_0 = 1.0$, which suggests the presence of macropores (> 50 nm). A wide distribution range of pore sizes from 10 to 100 nm can be observed in Fig. 5b. The specific surface areas and pore parameters of La-25 and La-150 are provided in Table 1. As we can see from SEM (Fig. 2) and TEM images (Fig. 3) that the nanorods do not contain mesopores and macropores. Therefore, the observed pores in Fig. 5b should originate from the aggregation of nanorods.[30] Table 1 also shows that the surface areas and pore volume of La-25 are lower than that of La-150.

Table 1 Summary of the specific surface areas, pore parameters and NO removal ratio of La-25 and La-150.

Samples	S_{BET} (m^2/g)	Total volume (cm^3/g)	Peak pore size (nm)	NO removal ratio (%)
La-25	33	0.245	3.6/25.9	48.1
La-150	55	0.512	2.4/45.2	15.9

3.3. Nature of oxygen vacancy and optical properties

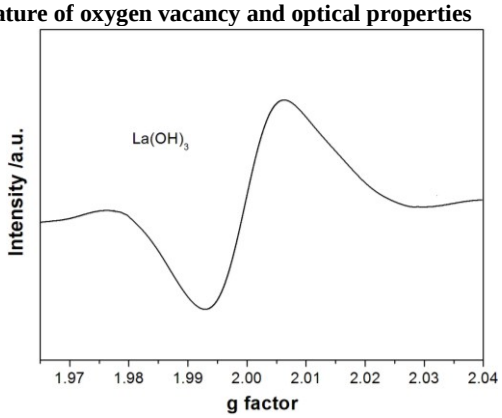

Fig. 6 Solid state ESR spectra of La-25 (T = 77K).

ESR could provide a sensitive and direct method to monitor various behaviors of defects.[29] To further confirm the nature of defects, electron spin resonance (ESR) measurement of La-25 sample was performed at 77 K. La-25 sample exhibits a dominant ESR signal at g~1.994, as can be seen from Fig. 6. As is reported, the oxygen vacancies should have signals closer to free electrons, i.e. 2.0.[32] The signal with g~1.994 is associated with the oxygen vacancies arising from free electrons.[32,33] Therefore, the ESR

signal which could be identified as the electrons trapped on oxygen vacancies.[34] These results reveal that surface oxygen-vacancies are generated during the preparation of $La(OH)_3$ by precipitation method, which is also consistent with HRTEM observation (Fig. 3c).

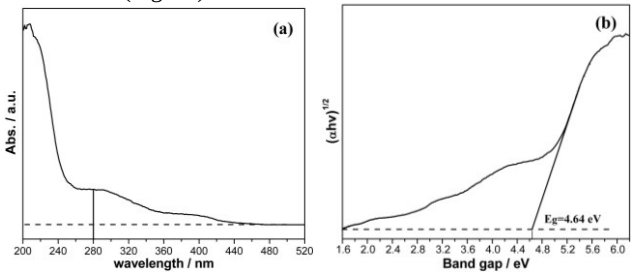

Fig. 7 UV-vis DRS (a) and plot of $(\alpha h\nu)^{1/2}$ versus photon energy (hν) (b) of La-25.

It's well known that the optical properties of the semiconductors are closely related to its photocatalytic activity. The optical property of the La-25 sample was examined by the UV–vis diffuse reflectance spectra (UV-vis DRS), as shown in Fig. 7a. The La-25 sample displays an onset of absorption at 265 nm, which can be assigned to the intrinsic band gap absorption of $La(OH)_3$. Further observation implies that La-25 sample exhibit the light absorption in the range of 280 to 420 nm, which may be attributed to the surface oxygen-vacancies resulting in a new conduction band.[35]

Band gap energies can be estimated from the UV-vis DRS. According to the lowest allowed electronic transition, semiconductors are classified to be direct or indirect. Direct semiconductors are characterized by the minimum of the lowest conduction band positioned in k space directly under the maximum of the highest valence band. The relation between absorption coefficient (α) and incident photon energy (*hν*) can be written as $\alpha = Bd\ (h\nu - Eg)^{1/2}/h\nu$, where Bd is the absorption constants.[36] Plots of $(\alpha h\nu)^{1/2}$ versus *hν* from the spectral data of Fig. 7a are presented in Fig. 7b. The intercept of the tangent to the plot will give a good approximation of the band gap energy for La-25. The direct band gap energies estimated from the intercept of the tangents to the plots is 4.64 eV.[37- 38]

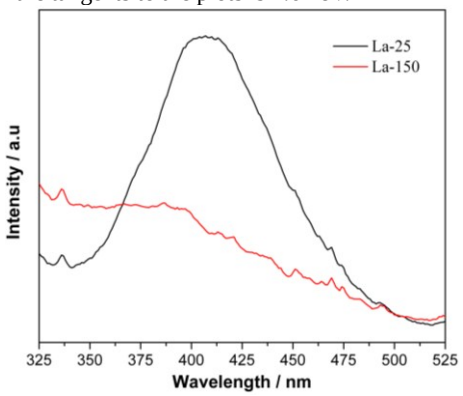

Fig. 8 Room temperature PL emission spectra of La-25 and La-150 at an excitation wavelength of 280 nm.

To further explore the nature of oxygen vacancy of $La(OH)_3$ nanorods, we carried out PL measurements at room temperature. As shown in Fig. 8, the La-150 exhibits almost no PL emission and La-25 has a high PL peak centered at 410 nm. The absorption energy La-25 is around 4.64 eV. Therefore, the emission of 410 nm could not contribute to the transition from the conduction band to the valence band, because the energy gap of 4.64 eV corresponds to the photoabsorption of 267 nm. The emission at 410 nm can be attributed a deep-level or trap-state emission. The emission transition can be ascribed to singly ionized oxygen vacancies in La-25. The emission should originate from the radiative recombination of a photogenerated hole with an electron occupying an oxygen vacancy.[6] The La-150 with high crystallinity dose not display PL emission because it contain little oxygen vacancy.

3.4. DFT Computation

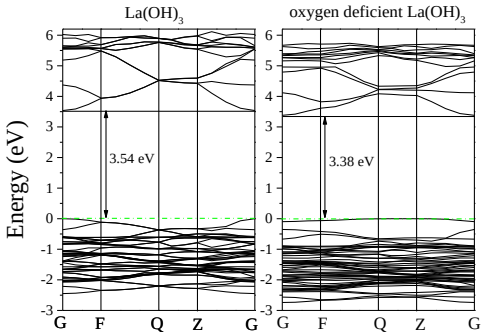

Fig. 9 The DFT band structure for La (OH)3 and oxygen deficient La(OH)3. (The energy zero is taken as the Fermi level and displayed with a green dashed line)

$La(OH)_3$ has a hexagonal crystal structure with space group P 63/m. The calculated lattice parameters of pure La $(OH)_3$ model are a = b = 6.696 Å and c = 3.892 Å at ambient conditions, which are in good agreement with experiment values of a = b = 6.529 Å and c = 3.852 Å.[39] These results indicate that our calculation methods are reasonable, and the calculated results are authentic. The formation energy of the oxygen vacancies in La $(OH)_3$ is 3.82 eV, which suggests the formation of oxygen vacancies in La $(OH)_3$ is easy.

The band structure of the $La(OH)_3$ and oxygen deficient $La(OH)_3$ is obtained by the DFT calculations, as shown in Fig. 9. The calculated band gap of pure La $(OH)_3$ is 3.54 eV, which is much smaller than the experimental band gap of 4.64 eV, due to the well-known shortcomings of GGA.[40-42] The calculated band gap of oxygen deficient $La(OH)_3$ is 3.38 eV. The position of valence band does not change. Due to calculation limitation, the original conduction band cannot be resumed. So, the observed bottom of conduction band for oxygen deficient $La(OH)_3$ should be new impurity level mediated by oxygen-vacancies, which is consistent with the UV-vis DRS observation (Fig. 7).

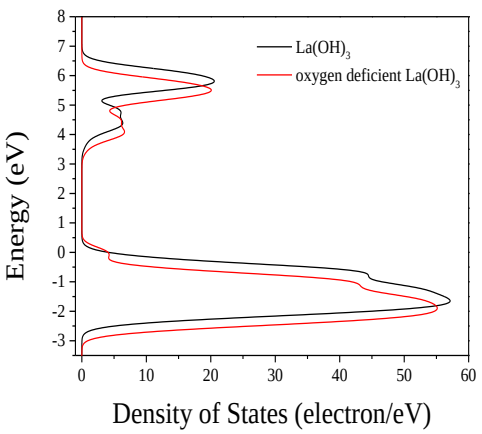

Fig. 10 The DFT total density of states for $La(OH)_3$ and oxygen deficient $La(OH)_3$.

To further understand the origin of the band gap variation, the total density of states (DOS) is calculated and plotted in Fig. 10 for La $(OH)_3$ and oxygen deficient $La(OH)_3$. Considering the calculation limitation, the oxygen-vacancy in La $(OH)_3$ induce impurity level within the band gap, which give a good explanation for the experimentally observed absorption at 280 nm. The formation of impurity level by oxygen vacancy is consistent with other oxygen deficient semiconductors.[43- 44]

3.5. Photocatalytic activity and mechanism of the $La(OH)_3$ nanorods

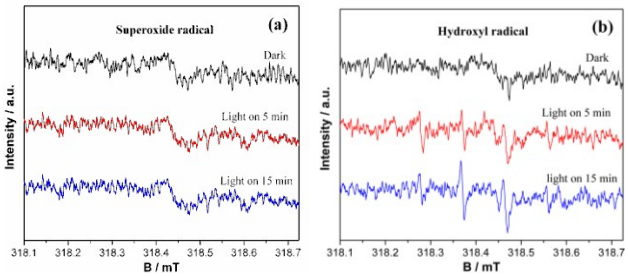

Fig. 11 DMPO spin-trapping ESR spectra of La-25 in methanol dispersion for $\bullet O^{2-}$ (a) and in aqueous dispersion for •OH (b).

It is important to determine the main oxidative species in the photocatalytic process for elucidating the photocatalysis mechanism.[45] ESR is a powerful technique for detection of photogenerated radicals in photocatalysis process.[46-48] DMPO (5, 5-dimethyl-1-pyrrolineN-oxide) are generally used for trapping radicals due to the generation of some stable radicals, such as DMPO-hydroxyl radical (•OH) and DMPO-superoxide radical ($\bullet O_2^-$). The ESR technique is employed to monitor the reactive species generated during the light irradiation of the La-25 with DMPO in methanol and water, and the results are shown in Fig. 11. The signals of superoxide ($\bullet O_2^-$) cannot be observed. However, the signals of the hydroxyl radical (•OH) could be observed when La-25 suspension is irradiated for 5 min by a pulsed laser system. Besides, the intensity of the •OH signal of La-25 increases considerably after irradiated for 15 min. Therefore, hydroxyl radical (•OH) are the main oxidative species for La-25 system. Considering the band structure of $La(OH)_3$, the conduction band position (-1.15 eV) is more negative than that of potential of $O_2/\bullet O_2^-$ (-0.33 eV), the $\bullet O_2^-$ should be produced. The generated $\bullet O_2^-$ can be rapidly transform to •OH, thus no $\bullet O_2^-$ signal can be detected. On the basis of the above results and analysis, we propose the pathway for generating active oxygen radicals (•OH) on the surface of La-25 as follows:

$$La(OH)_3 + UV \leftrightarrow h^+ + e^- \quad (1)$$
$$e^- + O_2 \rightarrow \bullet O_2^- \quad (2)$$
$$\bullet O_2^- + 2H^+ + e^- \rightarrow H_2O_2 \quad (3)$$
$$H_2O_2 + e^- \rightarrow \bullet OH + OH^- \quad (4)$$
$$h^+ + OH^- \rightarrow \bullet OH \quad (5)$$

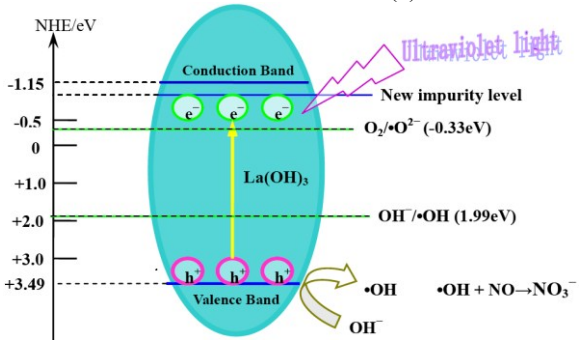

Fig. 12 photocatalytic mechanism scheme of La-25 under ultraviolet light irradiation.

The band edge positions of conduction band (CB) and valence band (VB) of semiconductor can be determined by the following approach. The VB edge potential of a semiconductor at the point of zero charge can be calculated by the following empirical equation: $E_{VB} = X - E_c + 0.5Eg$,[37, 49,50] where X is the absolute electronegativity of the semiconductor, Ec is the energy of free electrons on the hydrogen scale (about 4.5 eV), and Eg is the band gap energy. Moreover, conduction band (CB) edge potential (E_{CB}) can be determined by $E_{CB} = E_{VB} - Eg$. The calculated positions of CB and VB of La-25 are listed in Table 2. In combination with the experimental and calculation results, the potential of new CB is located below -0.94 eV.

Table 2 Absolute electronegativity, calculated CB edge, new CB position, calculated VB position and band gap energy for La-25 at the point of zero charge.

Sample	Absolute electronegativity (X) (eV)	Calculated CB position (eV)	New CB position (eV)	Calculated VB position (eV)	Band gap Energy (eV)
La-25	5.67	-1.15	Below -0.94	3.49	4.64

Based on the results above, the schematic electronic band structure, electron–hole generation and separation pathways under ultraviolet light irradiation are shown in Fig. 13. Under UV light irradiation, electron-hole pairs cannot be generated as the intrinsic band gap (4.64 eV) is too large. Instead, electron-hole pairs can be produced by transferring of electrons from the VB to the new impurity level of La-25. The photoexcited electrons of La-25 could reduce O_2 to $\bullet O_2^-$, and the generated $\bullet O_2^-$ can be transformed rapidly to •OH (Eq. 3 and 4). As all the $\bullet O_2^-$ radicals could transform into •OH radicals. Meanwhile, the potential of the holes at the VB of La-25 (3.53 eV) is more positive than the redox potential of $OH^-/\bullet OH$ (1.99 eV), and therefore the holes could directly oxidize OH^- to •OH. The •OH radicals as major reactive oxidation species could mineralize the pollutants to final products (Fig. 11b).[51- 52]

3.6 Photocatalytic activity and photochemical stability for NO removal

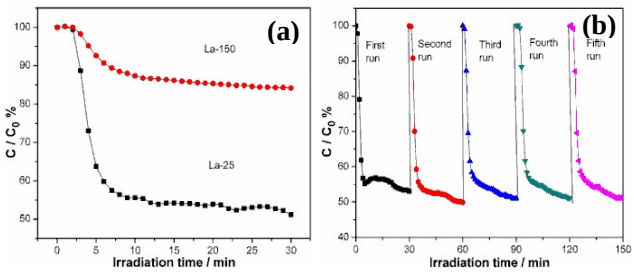

Fig. 13 Ultraviolet light photocatalytic activity of La-25 and La-150 samples (a), and repeated ultraviolet light photocatalytic runs of La-25 for the removal of NO in air (b).

The as-prepared $La(OH)_3$ nanorods are expected to exhibit high photocatalytic efficiency. Fig. 13a shows the variation of NO concentration (C/C_0%) with irradiation time over La-25

samples under ultraviolet light irradiation with La-150 as reference sample. Here, C_0 and C are the concentration of NO at time 0 and t min, respectively. The photolysis of NO can be negligible without the aid of the photocatalyst according to previous research.[53,54] The removal ratio of NO for 30 min by the La-25 and La-150 products is 48.1%, 15.9%, respectively, which indicates that the La-25 samples show a higher efficiency than the La-150 product (Fig. 13a). Notably, the high activity of La-25 sample can be attributed to the following factors. Firstly, the La-25 with the oxygen-vacancy shows extended UV light capture and conversion. Secondly, the one dimensional nanorods structure could facilitate the separation of photoinduced charge carriers.[55,56] The significant enhancement of UV photocatalytic activity of La-25 is mainly caused by the surface oxygen-vacancy states. As the La-150 prepared by hydrothermal method at high temperature has a high crystallinity with less surface oxygen-vacancies, the activity is therefore decreased.

As the •OH radicals are the major reactive species, the NO could react with the photogenerated •OH radicals generated from the photocatalytic reaction in the presence of the as-prepared photocatalyst to produce HNO_2 and HNO_3,[57-59] which involves the three reactions presented in the following Eqs. (6)–(8).

$$NO + 2{\bullet}OH \rightarrow NO_2 + H_2O \quad (6)$$
$$NO_2 + {\bullet}OH \rightarrow NO_3^- + H^+ \quad (7)$$
$$NO + NO_2 + H_2O \rightarrow 2\,HNO_2 \quad (8)$$

In order to put the as-prepared samples into practical applications, the photocatalytic stability of the samples is tested. An ideal photocatalyst should maintain photochemical and structural stability under repeated irradiation so that it can be used repetitively.[60-62] Fig. 13b shows the repeated photocatalytic runs of La-25 under UV light irradiation. It is significant to find that the photocatalytic efficiency of La-25 does not exhibit obvious loss after five recycles, indicating that the La-25 is relatively stable during the photocatalytic process. The photochemical stability of La-25 can be probably ascribed to special structure of 1D nanorod which could promote the transfer of reactants and products instead of accumulating on the surface, thus effectively preventing the photocatalyst from deactivation.

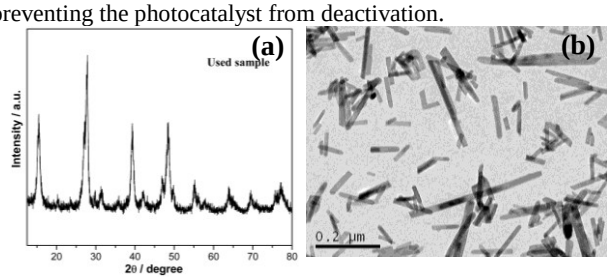

Fig. 14 XRD pattern (a) and TEM image (b) of La-25 after the cycling photocatalytic reactions.

The XRD patterns of La-25 after the repeated photocatalytic reactions have been measured as shown in Fig. 14a. It can be found that the La-25 after reaction exhibits a XRD pattern that is similar to the fresh sample (Fig. 1). Fig. 14b shows that the nanorod morphology of La-25 after reaction is almost identical to the fresh sample (Fig. 3a). Obviously, the crystal and morphological structures of the La-25 do not change after the photocatalytic reaction, which implies that the La-25 samples have an excellent structural and photochemical stability during repeated UV irradiation.

4. Conclusion

Uniform $La(OH)_3$ nanorods have been successfully fabricated by a fast, facile and scalable method using $La(NO_3)_3\,6H_2O$ and ammonia solution as precursors at room temperature. The synthesis procedure is very simple and can be finished within a short time. The $La(OH)_3$ nanorods exhibit high photocatalytic activity and stability for NO removal with a removal ratio of 48.1% under UV irradiation. The hydroxyl radicals were confirmed to be the dominant reactive species during photocatalysis. The high photocatalytic activity of La-25 nanorods is attributed to the presence of oxygen-vacancy and one dimensional nanostructure. The PL, ESR and DFT calculation confirms the role of oxygen-vacancy in formation of new impurity level, which endow the defective $La(OH)_3$ with extended UV light absorption and harvesting. This work could not only provide a simply and scalable strategy for fabrication of 1D $La(OH)_3$ nanorods but also new insights into the role of oxygen-vacancy in promoting photocatalysis efficiency.

Acknowledgements

This research is financially supported by the National Natural Science Foundation of China (51478070, 51108487), and the Science and Technology Project from Chongqing Education Commission (KJZH14210).

Phone/Fax: +86-23-62769785-605. E-mail: dfctbu@126.com (Fan Dong), jzma@rcees.ac.cn (Jinzhu Ma),

References

1 Z. L. Wang, *Adv. Mater.*, 2000, **12**, 171295.
2 J. T. Hu, T. W. Odom and C. M. Lieber, *Acc. Chem. Res.*, 1999, **32**, 435.
3 Q. Zhang, H. Wang, X. Jia, B. Liu and Y. Yang, *Nanoscale*, 2013, **5**, 7175.
4 L.L.Wang,J.N.Deng,Zh.Lou and T.Zhang, *J. Mater. Chem. A*, 2014, **2**, 10022.
5 G. R. Patzke, F. Krumeich and R. Nesper, *Angew. Chem., Int. Ed.*, 2002, **41**, 2446.
6 C. G. Hu, H. Liu, W. Dong, Y. Y. Zhang, G. Bao, C. S. Lao, and Z. L. Wang, *Adv. Mater.*, 2007, **19**, 470.
7 Y. Wang, S. Liu, Y. Cai, S. J. Deng, B. Q. Han, R. Han, Q. Li, and Y. D. *Ceram. Int.*, 2014, **40** , 5091.
8 M. P. Rosynek and D. T. Magnuson, *J. Catal.*, 1977, **46**, 402.
9 P. S. Kohli, M. Kumar, K. K. Raina and M. L. Singla, *J. Mater. Sci.-Mater. Electron.*, 2012, **23**, 2257.
10 B. Tang, J. C. Ge, C. J. Wu, L. H. Zhuo, J. Y. Niu, Z. Z. Chen, Z. Q. Shi and Y. B. Dong, *Nanotechnology*, 2004, **15**, 1273.
11 G. Jia, Y. Huang, Y. Song, M. Yang, L. Zhang and H. You, *Eur. J. Inorg. Chem.*, 2009, **2009**, 3721.
12 X. Wang and Y. D. Li, *Angew. Chem. Int. Ed.*, 2002, **41**, 4790.
13 Q. Mu, T. Chen and Y. Wang, *Nanotechnology*, 2009, **20**, 345602.
14 C. Wen, A. Yin, and W. Dai, *Appl. Catal. B-Environ.*, 2014, **160**, 730.
15 Z. Zhao, Y. Sun, and F. Dong, *Nanoscale*, 2015, **7**, 15.
16 F. Dong, X. Feng, Y. X. Zhang, C. F. Gao and Z. B. Wu, *RSC Adv.*, 2015, **5**, 11714.
17 M. K. Nowotny, L. R. Sheppard, T. Bak and J. Nowotny, *J. Phys. Chem. C*, 2008, **112**, 5275.
18 H. H. Pham, and L. W. Wang, *Phys. Chem. Chem. Phys.*, 2015, **17**, 541.
19 M. Kong, Y. Z. Li, X. Chen, T. T. Tian, P. F. Fang, F. Zheng and X. J. Zhao, *J. Am. Chem. Soc.*, 2011, **133**, 16414.
20 H. Y. Wang, G. M. Wang, Y. C. Ling, M. Lepert, C. C. Wang, J. Z. Zhang and Y. Li, *Nanoscale*,2012, **4**, 1463.
21 Z. Pei, L. Ding, W. Feng, S. Weng, and P. Liu, *Phys. Chem. Chem. Phys.*, 2014, **16**, 21876.
22 G. M. Wang, H. Y. Wang, Y. C. Ling, Y. C. Tang, X. Y. Yang, R. C. Fitzmorris, C. C. Wang, J. Z. Zhang and Y. Li, *Nano Lett.*, 2011, **11**, 3026.
23 Y. C. Ling, G. M. Wang, J. Reddy, C. C. Wang, J. Z. Zhang and Y. Li, *Angew. Chem. Int. Ed.*, 2012, **51**, 4074.

24 Y. H. Lv, C. S. Pan, X. G. Ma, R. L. Zong, X. J. Bai and Y. F. Zhu, *Appl. Catal. B*, 2013, **26**, 138.
25 L. Q. Jing, F. L. Yuan, H. G. Hou, B. F. Xin, W. M. Cai and H. G. Fu, *Sci. China, Ser. B*, 2005, **48**, 25.
26 X. H. Lu, G. M. Wang, S. L. Xie, J. Y. Shi, W. Li, Y. X. Tong and Y. *Chem. Commun.*, 2012, **48**, 7717.
27 M. C. Yan, F. Chen, J. L. Zhang and M. Anpo, *J. Phys. Chem. B*, 2005, **109**, 8673.
28 D. M. Chen, Z.H. Wang, T. Zh. Ren, H. Ding, Y. F. Zhu, *J. Phys. Chem. C*, 2014, **118**, 15300.
29 H. Wong, H. Iwai, K. Kakushima, B. L. Yang and P. K. Chu, *J. Electrochem. Soc.*, 2010, **157**, G49.
30 J.G. Yu, Q. J. Xiang and M. H. Zhou, *Appl. Catal. B*, 2009, **90**, 595.
31 K. A. Alim, V. A. Fonoberov, M. Shamsa and A. A. Balandina, *J. Appl. Phys.*, 2005, **97**, 124313.
32 A. B. Djurišić, W. C. H. Choy, V. A. L. Roy, Y. H. Leung, C. Y. Kwong, K. W. Cheah, T. K. Gundu. Rao, W. K. Chan, H. L. Fei and C. Surya, *Adv. Funct. Mater.*, 2004, **14**, 856.
33 S. B. Zhang, S. H. Wei and A. Zunger, *Phys. Rev. B*, 2001, **63**, 075205.
34 I. Nakamura, N. Negishi, S. Kutsuna, T. Ihara, S. Sugihara and K. Takeuchi, *J. Mol. Catal. A: Chem.*, 2000, **161**, 205.
35 J. Zh. Ma, H. M. Wu, Y. Ch. Liu and H. He, *J. Phys. Chem. C*, 2014, **118**, 7434.
36 F. Dong, W. R. Zhao and Zh. B. Wu, *Nanotechnology*, 2008, **19**, 365607.
37 H. Q. Jiang, M. Nagai and K. Kobayashi, *J. Alloys Compd.*, 2009, **479**, 821.
38 Z. B. Wu, F. Don, Y. Liu and H. Q. Wang, *Catal. Commun.*, 2009, **11**, 82.
39 I. Khidirov and V. T. Om, *Phys. Status Solidi A*, 1993, **140**, 59.
40 J. P. Perdew and M. Levy, *Phys. Rev. Lett.*, 1983, **51**, 1884.
41 C. Stampfl and C. G. Van de Walle, *Phys. Rev. B*, 1999, **59**, 5521.
42 R. W. Godby, M. Schlter and L. Sham, *J. Phys. Rev. B*, 1988, **37**, 10159.
43 F. C. Lei, Y. F. Sun, K. T. Liu, Sh. Gao, L. Liang, B. C. Pan and Y. Xie, *J. Am. Chem. Soc.*, 2014, **136**, 6826.
44 L. J. Chen, Y. J. Zhao, J. Y. Luo and Y. Y. Xia, *Phys. Lett. A*, 2011, **375**, 934.
45 S. K. Muduli, S. Wang, S. Chen, C. F. Ng, C. H. A. Huan, T. C. Sum and H. S. Soo, *Beilstein J. Nanotechnol.*, 2014, **5**, 517.
46 H. B. Fu, C. S. Pan, W. Q. Yao and Y. F. Zhu, *J. Phys. Chem. B*, 2005, **109**, 22432.
47 T. G. Xu, L. W. Zhang, H. Y. Cheng and Y. F. Zhu, *Appl. Catal. B*, 2011, **101**, 382.
48 T. Xia, Y.L. Zhang, J. Murowchickc, X.B. Chen, *Catal.Today*, 2014, **225**, 2.
49 X. Zhang, L. Z. Zhang, T. F. Xie and D.J. J. Wang, *Phys. Chem. C*, 2009, **113**, 7371.
50 O. Xiao, J. Zhang, C. Xiao and X. K. Tan, *Catal. Commun.*, 2008, **9**, 1247.
51 D. Li, X. J. Bai, J. Xu, X. G. Ma and Y. F. Zhu, *Phys. Chem. Chem. Phys.*, 2014, **16**, 212.
52 C. C. Chen, X. Z. Li, W. H. Ma and J. C. Zhao, *J. Phys. Chem. B*, 2002, **106**, 318.
53 F. Dong, Q. Y. Li, Y. J. Sun and W. K. Ho, *ACS Catal.*, 2014, **4**, 4341.
54 F. Dong, Z. Y. Wang, Y. H. Li, W. K. Ho and S. C. Lee, *Environ. Sci. Technol.*, 2014, **48**, 10345.
55 Z. R. Tang, X. Yin, Y. H. Zhang and Y. J. Xu, *RSC Adv.*, 2013, **3**, 5956.
56 J. Liang, Y. Q. Cao, H. Lin, Z. Zh. Zhang, Ch. C. Huang and X. X. Wang, *Inorg. Chem.*, 2013, **52**, 6916.
57 F. Dong, H. T. Liu, W. K. Ho, M. Fu, and Z. B. Wu, *Chem. Eng. J.*, 2013, **214**, 198.
58 X. Ding, X. Song, P. N. Li, Z. H. Ai and L. Z. Zhang, *J. Hazard. Mater.*, 2011, **190**, 604.
59 Y. Zhou, X. J. Zhang, Q. Zhang, F. Dong, F. Wang and Z. Xiong, *J. Mater. Chem. A*, 2014, **2**, 16623.
60 F. Dong, T. Xiong, Y. J. Sun, Y. X. Zhang and Y. Zhou, *Chem. Commun.*, 2015, **51**, 8249.
61 T. Xiong, H. W. Huang, Y. J. Sun, and F. Dong, *J. Mater. Chem. A*, 2015, **3**, 6118.
62 Z. Y. Wang, W. Guan, Y. J. Sun, F. Dong, Y. Zhou and W. K. Ho, *Nanoscale*, 2015, **7**, 2471.